# Ultrathin Amorphous Nickel Doped Cobalt Phosphates with Highly Ordered Mesoporous Structures as Efficient Electrocatalyst for Oxygen Evolution Reaction

*Lan Yang, Hao Ren, Qinghua Liang, Khang Ngoc Dinh, Raksha Dangol and Qingyu Yan**

L. Yang, Dr. H. Ren, Dr. Q. Liang, K. N. Dinh, R. Dangol, Prof. Q.Y.Yan

School of Materials Science and Engineering

Nanyang Technological University

Singapore 639798, Singapore

E-mail: alexyan@ntu.edu.sg

Keywords: cobalt phosphate, nickel doping, amorphous mesoporous, oxygen evolution reaction, electrocatalysts

Herein, the authors report the facile preparation of ultrathin (≈3.8 nm in thickness) two-dimensional (2D) cobalt phosphate (CoPi) nanoflakes through an oil-phase method. The obtained nanoflakes are composed of highly ordered mesoporous (≈3.74 nm in diameter) structure and exhibits an amorphous nature. Attractively, when doped with nickel, such 2D mesoporous Ni-doped CoPi nanoflakes display decent electrocatalytic performances in terms of intrinsic activity, low kinetic barrier towards oxygen evolution reaction (OER). Particularly, the optimized 10 *at*% Ni-doped CoPi nanoflakes (denoted as Ni10-CoPi) delivers a low overpotential at 10 mA $cm^{-2}$ (320 mV), small Tafel slope (44.5 mV $dec^{-1}$) and high stability for OER in 1.0 M KOH solution, which is comparable to the state-of-the-art $RuO_2$ tested in the same condition (overpotential: 327 mV at 10 mA $cm^{-2}$, Tafel slope: 73.7 mV $dec^{-1}$). The robust framework coupled with good OER performance enable the 2D mesoporous Ni10-CoPi nanoflakes to be promising material for energy conversion applications.

## 1. Introduction:

Owing to the depletion of fossil fuel and increasing concern on global warming, there is an urgent desire for sustainable and clean energy resources. Hydrogen is named as one to the most promising candidate, which could be produced from water electrolysis.[1] The main challenge

is that the anodic reaction of water splitting - oxygen evolution reaction (OER) exhibits sluggish kinetics and high activation barrier (overpotential) because it involves four electron-electron process and O=O bond formation. Highly active electrocatalysts is needed to fasten reaction kinetics and lower that overpotential. However, the benchmark OER catalyst so far still based on the expensive and low-abundance noble metals such as $IrO_2$ and $RuO_2$.[2]

The past decade has witnessed extraordinary progress on overcoming the bottleneck of OER electrocatalysis by transition metal phosphides,[3] dichalcogenides,[4] nitrides,[5] and thiophosphate materials.[6] Nevertheless, the real active sites of the above materials remain controversial because their phase, structure, and composition usually undergo obvious change under strong oxidation condition.[3c, 7] It has been reported that the phosphate group plays an important role in facilitating adsorption and stabilizing catalytic centers,[8] however transition metal phosphates are rarely explored as electrocatalysts for OER. Among the few reports on phosphate materials as OER catalyst, their performances are far from satisfactory.[8c, 9] As known, the electrocatalytic performance depends on many factors, such as the number of accessible active sites, mass transport efficiency, and the ability to resist corrosion in electrolytes, which are related to the internal compositional properties as well as the external structure and morphology.[3c, 10]

Hence, there are multiple effective strategies to optimize the OER performance of transition metal phosphates. First, cation doping can improve the intrinsic activity. Mixed metal cations show more favourable adsorption/desorption of oxygen-containing intermediates than that of the single-metal counterparts.[8b, 8c] The transition metal Fe, Co, Ni and their compounds are excellent catalysts in alkaline OER reactions, and different combinations of these three elements can significantly change the properties of the catalysts. It was reported that moderate amount of Fe and Ni doping in cobalt-based catalysts yields good OER activity and low overpotential, which are associated with reduction of the adsorption energy on the catalyst

surface.[11] Due to the similar atomic structure of Co and Ni subgroup elements, Ni doping in CoPi is beneficial to keep the original morphology and structure. Moreover, reducing the thickness is another effective way since it can accelerate the mass transport.[12] Mass transport is an important parameter to describe the transfer rate of electrocatalysts to the electrolyate. Faster mass transport leads to higher electrocatalysts utilization, which means better performance of the electrocatalysts for the same mass loading.[13] Furthermore, highly-ordered porous structure such as mesopores can offer higher surface area, which means more active sites are exposed to electrolyte.[14] The increased effectively active surface area facilitates the adsorption/desorption process and yields better electrocatalytic activity. Last but not least, the design of amorphous structure has merits such as short-range structure ordering and high active sites density.[15] Compared to crystallized materials, the disordered structures of amorphous electrocatalysts offer more active sites for highly efficient water oxidation.

In consideration of the above merits, herein, a facile oil-phase method is employed to realize the compositional, morphological, and lattice structural engineering of transition metal phosphates. Particularly, the amorphous 10 *at*% Ni doped CoPi nanoflakes (denoted as Ni10-CoPi) composed of highly ordered mesoporous structure were prepared as an efficient and electro-stable OER electrocatalyst. The obtained mesoporous Ni10-CoPi nanoflakes show an ultrathin thickness of 3.8 nm and an average pore diameter of 3.74 nm. During OER process, the as-prepared Ni10-CoPi electrodes show a decent activity with low overpotential of 320 mV at 10 mA $cm^{-2}$ and small Tafel slope of 44.5 mV $dec^{-1}$.

## 2. Results and discussion

We prepared the mesoporous CoPi nanoflakes with different Ni doping content of 0%, 5%, 10% and 15% based on a modified oil-phase method (see Experimental Section for details).[16] The Co/Ni atomic ratio of the as-obtained CoPi, Ni5-CoPi, Ni10-CoPi and Ni15-CoPi was

confirmed by individually coupled plasma-optical emission spectrometry (ICP-OES), which is close to what were used in the corresponding synthesis (**Table S1, Supporting Information**).

X-ray diffraction (XRD) patterns of the synthesized CoPi, Ni5-CoPi, Ni10-CoPi and Ni15-CoPi (**Figure 1a**) show no diffraction peak, indicating the amorphous nature of the tested samples. To investigate the chemical bonds and oxidation states of the obtained materials, X-ray photoelectron spectroscopy (XPS) was performed on CoPi and Ni10-CoPi (Figure 1b-d; **Figure S1, Supporting Information**). In the high-resolution Co 2p XPS spectrum (Figure 1b), the spin-orbit doublets of Co $2p_{3/2}$ and Co $2p_{1/2}$ are located at binding energy of 797.4 and 781.64 eV, respectively. The spin energy interval is around 16.76 eV, suggesting the existence of $Co^{2+}$.[17] In the corresponding Ni 2p profile (Figure 1c), the main two peaks observed at the binding energy of 856.23 eV and 873.88 eV can be attributed to Ni $2p_{3/2}$ and Ni $2p_{1/2}$ from the $Ni^{2+}$ species, respectively.[18] The P 2p (Figure 1d) and O 1s (Figure S1b, Supporting Information) XPS spectra show the feature peaks at 132.76 eV and 531.2 eV, respectively, which matches the characteristic peaks of $(PO_4)^{3-}$.[19]

The low-magnification transmission electron microscopy (TEM) images clearly reveal the nanoflakes morphology of Ni10-CoPi with a lateral size of > 800 nm (**Figure 2a**). Furthermore, the high-resolution TEM (HRTEM) images in Figure 2b-c show that there are many channels on the nanoflakes. The distance between the centres of two neighbouring channels (defines as $D_{center}$) is measured to be ~3.74 nm (inset of Figure 2c), indicating the mesoporous structure of the obtained material. HRTEM images of CoPi, Ni5-CoPi, and Ni15-CoPi (**Figure S2, Supporting Information**) show the same mesoporous morphology and very similar pore diameters of ~3.42 nm, ~3.4 nm and ~3.75 nm, respectively. The selected area electron diffraction (SAED) pattern (inset of Figure 2b) further confirmed the amorphous nature of the material, which agrees well with the XRD result above. The low-angle X-ray diffraction (XRD) in Figure 2d shows three resolved diffraction peaks. According to Bragg's law ($2d \sin\theta = n\lambda$),

the *d* values for the three peaks are calculated to be 1.87, 1.26 and 0.94 nm. The three *d* values is approximately ½, $^1/_3$, ¼ of the $D_{center}$, thus indicating that the three peaks can be accordingly indexed as (200), (300) and (400) reflections and proves that the mesopores are highly ordered distributing along the [100] direction. The low-angle XRD patterns of Co-Pi, Ni5-CoPi and Ni15-CoPi nanoflakes (**Figure S3, Supporting Information**) also show the same connection between the *d* values and $D_{centre}$, indicating that doping of Ni did not affect the structure and morphology of the synthesized materials. It is worth noting that the thickness of the flake measured by atomic force microscopy (AFM) (~3.8 nm, **Figure S4, Supporting Information**) is very close to *d* and $D_{center}$, indicating that the nanoflake may contain only one layer of the mesoporous channels. The ultrathin nature of the materials is conducive to mass transport and charge transfer, which leads to high electrocatalytic performance towards water oxidation. Moreover, the energy dispersive X-ray spectroscopy (EDX) elemental mapping confirmed the presence of P, Co, and Ni and their uniform distribution overlapping the Ni10-CoPi nanoflakes, which is consistent with the XPS results (**Figure S5, Supporting information**).

To investigate the electrocatalytic performance of Ni10-CoPi, we tested the Ni10-CoPi nanoflakes for OER in the alkaline solution of 1.0 M KOH. A three-electrode system was used with a glassy-carbon electrode coated with catalyst as the working electrode, carbon rod and Hg/HgO as the contact and reference electrode respectively. The OER activities of CoPi, Ni5-CoPi, Ni15-CoPi, and $RuO_2$ were also evaluated for comparison.

In the iR-compensated polarization curves obtained by steady-state linear sweep voltammetry (LSV) (**Figure 3a**), it can be seen that the Ni10-CoPi electrode exhibits an onset overpotential of 273 mV, which is obviously lower than those of CoPi (303 mV), Ni5-CoPi (287 mV) and Ni15-CoPi (280 mV). Moreover, Tafel slopes obtained from Tafel equation indicate that Ni10-CoPi electrode has faster OER kinetics with a smaller Tafel slope of 44.5 mV $dec^{-1}$. The Tafel slope of CoPi, Ni5-CoPi and Ni15-CoPi is 68.3 mV $dec^{-1}$, 55.1 mV $dec^{-1}$, and 51.2 mV $dec^{-1}$,

respectively (Figure 3b). Besides, this performance also surpasses the tested OER electrocatalyst $RuO_2$, which requires 327 mV to drive a current density of 10 mA $cm^{-2}$ and the corresponding Tafel slope is 73.7 mV $dec^{-1}$ (Figure S6, Supporting Information). The respective $\eta_{10}$, i.e., required overpotential to realize the current density of 10 mA $cm^{-2}$, for the optimized Ni10-CoPi nanoflakes is 320 mV, which is less than that of CoPi (354 mV), Ni5-CoPi (335 mV) and Ni15-CoPi (325 mV) (Figure 3c). More importantly, the chronoamperometry test shows that a stable current density of 20 mA $cm^{-2}$ is maintained for 20 h with ignorable change less than 5%, demonstrating the excellent durability of the electrode (Figure 3d). The XRD characterization shows that the Ni10-CoPi electrode still maintains the amorphous structure after 20-hour stability test (**Figure S7a, Supporting Information**), indicating the structural stability during the OER process. For TEM analysis of Ni10-CoPi after stability test, the as-prepared electrode was dispersed into ethanol by vigorous sonication and then dropped onto the copper grid. Figure S7b-c in the Supporting Information show that after 20h OER, there are still some residual mesoporous structure (inset of Figure S7c, Supporting Information), indicating the morphology robustness. On the other hand, it is undeniable that the morphology of the Ni10-CoPi electrode was mostly damaged, which might be attributed to the formation of oxyhydroxide under highly oxidizing OER condition. To specify, post mortem XPS was carried out. As shown in Ni 2p XPS profile in **Figure S8a (Supporting Information)**, the two separate peaks appear at the binding energy of 861.83 eV and 855.15 eV, respectively, indicating the $Ni^{2+}$ and $Ni^{3+}$ states.[20] The corresponding peaks of $Co^{2+}$ and $Co^{3+}$ in Co 2p spectrum (Figure S8b, Supporting Information) appear at 781.50 eV and 779.80 eV, respectively.[21] Noteworthy, the atomic ratio of $Ni^{2+}/Ni^{3+}$ and $Co^{2+}/Co^{3+}$ are all 5:4, indicating that the doped Ni were equally oxidized as Co during OER and played as important role as Co in the electrocatalytic process. Figure S8c in Supporting Information shows that after OER, P became very less. In contrast, the O 1s spectrum (Figure S8d, Supporting Information)

expanded after 20 h OER, indicating that O content increased. The atomic ratio of P/O is 96.36:0.84 after XPS analysis. Furthermore, the two corresponding peaks in the O 1s profile indicate that the ratio of $OH^-$:$O^{2-}$ (at 531.3 and 533.2 eV, respectively) is 2:1, which proved our previous assumption about oxyhydroxide formation.[22]

The electrochemically effective surface area (ECSA) was estimated to better understand the electrocatalytic properties of the Ni10-CoPi catalyst toward OER by conducting cyclic voltammetry (CV) at various scan rate (**Figure S9, Supporting Information**). The linear fit results in **Figure 4a** reveal that the Ni10-CoPi has a double layer capacitance ($C_{dl}$) value of 465.4 μF $cm^{-2}$, which is higher than that of CoPi (294.6 μF $cm^{-2}$), Ni5-CoPi (429.8 μF $cm^{-2}$) and Ni15-CoPi (274.7 μF $cm^{-2}$). Employing the $C_{dl}$ values, symbolic ECSA can be calculated.[23]The Ni10-CoPi nanoflakes displays an ECSA of 11.6 $m^2$, which is higher than that of CoPi (7.4 $m^2$), Ni5-CoPi (10.7 $m^2$) and Ni15-CoPi (6.9 $m^2$). This implies the higher density of active sites in Ni10-CoPi nanoflakes, which contributes to the high electrocatalytic activity. Furthermore, the specific activity (normalized to ECSA) were also calculated to investigate the origin of the superior performance of Ni10-CoPi (**Figure S10, Supporting Information**). Among the four electrodes, the Ni10-CoPi sample shows the highest specific activity of 0.52 mA $cm_{ECSA}^{-2}$ at the 380 mV OER overpotential, which outperforms those of CoPi (0.16 mA $cm_{ECSA}^{-2}$), Ni5-CoPi (0.22 mA $cm_{ECSA}^{-2}$) and Ni15-CoPi (0.46 mA $cm_{ECSA}^{-2}$). The higher specific activity indicates that Ni10-CoPi has higher intrinsic activity, which contributes to the better electrochemical performance. We also tested the electrochemical impedance spectroscopy (EIS) of the four samples (Figure 4b) to investigate the charge transfer ability of the materials. The charge transfer resistance ($R_{ct}$) of the Ni10-CoPi electrode is 38.59 Ω, which is much smaller than those of CoPi (190.5 Ω), Ni5-CoPi (92.17 Ω) and Ni15-CoPi (44.25 Ω). The smaller $R_{ct}$ indicates its faster charge transfer kinetics of the optimised Ni10-CoPi electrode.

## 3. Conclusion

In conclusion, the amorphous Ni10-CoPi nanoflakes composed of highly ordered mesoporous structure were prepared by a facile oil-phase method and demonstrated for the application of OER. The amorphous structure and mesoporous morphology provides high active sites density and large exposed surface area. The materials displayed its decent OER performance as seen by delivering a durable current density of 10 mA $cm^{-2}$ at 320 mV. Its reaction kinetics is comparable to noble metal based electrocatalyst such as Ir/RuOx with a gentle Tafel slope of only 44.5 mV $dec^{-1}$. The mesoporous Ni10-CoPi shows promise as a low-cost alternative due to its abundance as compared to Ru and Ir.

## 4. Experimental section

*Materials:* Cobalt (II) chloride hexahydrate ($CoCl_2 \cdot 6H_2O$, 98%), Nickel (II) Chloride Hexahydrate ($NiCl_2 \cdot 6H_2O$, 98%), sodium oleate (NaOA, ≥ 82% fatty acids (as oleic acid) basis powder), 1-Octadecene (ODE, technical grade, 90%), Tetradecylphosphonic acid (TDPA, 97 %) and Nafion®117 solution (5%, in a mixture of lower aliphatic alcohols and water) were purchased from Sigma-Aldrich. The isopropyl alcohol (IPA, technical grade, 99%), ethanol absolute (99.9%), hexane (99.9%) and methanol (99.9%) were purchased from Aik Moh. All chemicals and materials were used without further purification.

*Synthesis of $Co(OA)_2$ and Ni-doped $Co(OA)_2$ Precursor:* The synthesis of $Co(OA)_2$ and Ni-doped $Co(OA)_2$ precursor was followed by thermal decomposition. According to a typical method,[24] different molar ratio of Co/Ni solution (1:0, 95:5, 90:10, 85:15 for the synthesis of $Co(OA)_2$ and 5%, 10 %, 15% Ni-doped $Co(OA)_2$, respectively) were obtained by adding $CoCl_2 \cdot 6H_2O$, $NiCl_2 \cdot 6H_2O$ and 20mmol NaOA in a mixture solution of 16 mL ethanol absolute, 12 mL DI water and 28 mL hexane. The total amount of metal cations ($Co^{2+}$and $Ni^{2+}$) were kept at 10 mmol. Then the solution was heated at 70 ℃ for 4 hours with vigorous stirring. The

obtained products were firstly dissolved into hexane and then washed with deionized water (DI water) for 3 times and subsequently washed with methanol for 3 times. The pure brown $Co(OA)_2$ and Ni-doped $Co(OA)_2$ precursors were then dried at 80 ℃ in an vacuum oven overnight.

*Synthesis of Amorphous CoPi and Ni-doped CoPi nanoflakes with highly Ordered Mesoporous Structure:* The synthesis is based on a slightly modified oil-phase method.[16] To start, 5mL of ODE was heated to 300 ℃ under Ar protection in a three-neck flask. Next 0.9mmol $Co(OA)_2$ precursor and 0.6mmol TDPA were added into the hot oil and kept heating at 300 ℃ for 1.5 hours. Then cooled to room temperature naturally. Ni-doped CoPi was conducted with similar procedure by replacing $Co(OA)_2$ with Ni-doped $Co(OA)_2$. The obtained products were washed by hexane and IPA for 5 to 6 times and collected by centrifuging and dried in air.

*Characterizations:* The morphology of the samples was characterized with a transmission electron microscope (TEM) system (JEOL 2010 UHR), operating at 200 kV. X-ray diffraction was performed to characterize the samples on a Bruker D8 Advance powder X-ray diffraction (XRD) at the 2θ range of 10° to 80° with Cu Kα (λ = 1.5406 Å) radiation. The scanning rate is 2° $min^{-1}$ with a step size of 0.01°. Low-angle X-ray diffraction (XRD) was tested by Panalytical XPert Pro at the 2θ range of 3° to 10° with Cu Kα (λ = 1.5406 Å) radiation. X-ray photoelectron spectroscopy (XPS) was conducted on an ESCALAB 250 photoelectron spectroscopy (Thermo Fisher Scientific) using monochromatic Al Kα X-ray beam(1486.6 eV). The voltage step size was 1 eV for survey spectra and 0.1 eV for high resolution scan. The energy-dispersive X-ray spectroscopy (EDX) mapping was tested on a transmission electron microscopes (TEM, JEOL 2100HR). The composition of the synthesized materials was confirmed by the PerkinElmer Optima 8000 ICP-OES. AFM Asylum Research Cypher S was used to confirm the thickness of the obtained materials.

*Electrochemical Measurement:* For OER testing, 2.5 mg of the catalyst materials was dispersed in 0.5 mL of solution containing 485 µL of IPA and 15 µL of 5 wt% Nafion followed by ultrasonication for 30 minutes. Then, 10 µL of the prepared suspension was pipetted onto a pre-polished glassy carbon (GC) disk electrode (3 mm in diameter), followed by drying at room temperature for 5 minutes. Electrochemical measurements were performed in a typical three-electrode system on an electrochemical station (Solartron). A Graphite rod and Hg/HgO served as the counter electrode and the reference electrode, respectively. The catalyst-loaded GC electrode was used as the working electrode. All measurements were carried out in 1.0 M KOH electrolyte under room temperature. Linear sweep voltammetry (LSV) was conducted at a scan rate of 2 mV $s^{-1}$. In all measurements, Hg/HgO RE was calibrated: $E$(RHE)= $E$(Hg/HgO) + 0.059pH + 0.098. All LSV curves were corrected with 90% iR-compensation. By plotting overpotential $\eta$ *vs*. logarithm of current density from polarization curves, Tafel slopes were obtained.

EIS measurements were were carried out at a potential of 1.57 V (vs. RHE) in the frequency range from 100 KHz to 0.1 Hz in 1.0 M KOH solution. The electrochemically effective surface area (ECSA) was estimated from the electrochemical double-layer capacitance ($C_{dl}$) of the materials. The $C_{dl}$ was determined by a simple CV method. The CV was conducted in a potential window of -0.14~-0.04 V (vs. Hg/HgO reference electrode) at various scan rate of 10 mV $s^{-1}$, 20 mV $s^{-1}$, 40 mV $s^{-1}$, 60 mV $s^{-1}$, 80 mV $s^{-1}$ and 100 mV $s^{-1}$. For CoPi, Ni5-CoPi and Ni15-CoPi, the potential window is -0.19~-0.09 V, -0.16~-0.06 V and -0.17~-0.07 V, respectively. Then by plotting capacitive current difference $\Delta j = ja - jc$ at -0.14 V for CoPi, -0.11 V for Ni5-CoPi, -0.09 V for Ni10-CoPi, and -0.12 V for Ni15-CoPi against scan rates, an obtained linear slope is equivalent to twice of the double layer capacitance ($C_{dl}$) value. ECSAs were obtained from $C_{dl}$ values divided by 40 mA $cm_{ECSA}^{-2}$.

**Supporting Information**
Supporting Information is available from the Wiley Online Library or from the author.

**Acknowledgements**
This study was financially supported by Singapore MOE AcRF Tier 1 Grant 2016-T1-002-065, and Tier 2 under Grant Nos. 2017-T2-2-069 and 2018-T2-01-010. The authors greatly thank the Facility for Analysis, Characterization, Testing and Simulation (FACTS) of Nanyang Technological University, Singapore, for using their TEM, SEM, and XRD equipment.

References

1. (a) S. Chu,A. Majumdar, *Nature* **2012,** *488* (7411), 294-303, (b) T. R. Cook, D. K. Dogutan, S. Y. Reece, Y. Surendranath, T. S. Teets, D. G. Nocera, *Chem. Rev* **2010,** *110* (11), 6474-6502, (c) J. A. Turner, *Science* **2004,** *305* (5686), 972-974.

2. (a) R. Frydendal, E. A. Paoli, B. P. Knudsen, B. Wickman, P. Malacrida, I. E. L. Stephens, I. Chorkendorff, *ChemElectroChem* **2014,** *1* (12), 2075-2081, (b) Y. Lee, J. Suntivich, K. J. May, E. E. Perry, Y. Shao-Horn, *J. Phys. Chem. Lett* **2012,** *3* (3), 399-404, (c) T. Reier, M. Oezaslan, P. Strasser, *ACS Catal.* **2012,** *2* (8), 1765-1772, (d) M. Vuković, *J. Appl. Electrochem* **1987,** *17* (4), 737-745.

3. (a) C. G. Read, J. F. Callejas, C. F. Holder, R. E. Schaak, *ACS Appl. Mater. Interfaces* **2016,** *8* (20), 12798-12803, (b) J. Masud, S. Umapathi, N. Ashokaan, M. Nath, *J. Mater. Chem. A* **2016,** *4* (25), 9750-9754, (c) N.-T. Suen, S.-F. Hung, Q. Quan, N. Zhang, Y.-J. Xu, H. M. Chen, *Chem. Soc. Rev* **2017,** *46* (2), 337-365.

4. (a) J. Wu, M. Liu, K. Chatterjee, K. P. Hackenberg, J. Shen, X. Zou, Y. Yan, J. Gu, Y. Yang, J. Lou, P. M. Ajayan, *Adv. Mater. Interfaces* **2016,** *3* (9), 1500669, (b) X. Duan, J. Xu, Z. Wei, J. Ma, S. Guo, H. Liu, S. Dou, *Small Methods* **2017,** *1* (11), 1700156.

5. (a) J. Xie,Y. Xie, *Chem.: Eur. J.* **2016,** *22* (11), 3588-3598, (b) A. K. Tareen, G. S. Priyanga, K. Khan, E. Pervaiz, T. Thomas, M. Yang, *ChemSusChem* **2019,** *12* (17), 3941-3954,

(c) M.-S. Balogun, Y. Huang, W. Qiu, H. Yang, H. Ji, Y. Tong, *Mater. Today* **2017,** *20* (8), 425-451.

6. (a) P. Liu, R. N. Ali, J. Li, G. Hu, X. Zhu, Y. Lu, B. Xiang, *Appl. Surf. Sci* **2019,** *484*, 54-61, (b) Q. Liang, L. Zhong, C. Du, Y. Luo, Y. Zheng, S. Li, Q. Yan, *Nano Energy* **2018,** *47*, 257-265, (c) Q. Liang, L. Zhong, C. Du, Y. Luo, J. Zhao, Y. Zheng, J. Xu, J. Ma, C. Liu, S. Li, Q. Yan, *ACS Nano* **2019,** *13* (7), 7975-7984.

7. Y. Jiao, Y. Zheng, M. Jaroniec, S. Z. Qiao, *Chem. Soc. Rev* **2015,** *44* (8), 2060-2086.

8. (a) K. Jin, J. Park, J. Lee, K. D. Yang, G. K. Pradhan, U. Sim, D. Jeong, H. L. Jang, S. Park, D. Kim, N.-E. Sung, S. H. Kim, S. Han,K. T. Nam, *J. Ame. Chem. Soc* **2014,** *136* (20), 7435-7443, (b) Y. Li, C. Zhao, *Chem. Mater* **2016,** *28* (16), 5659-5666, (c) Y. Zhan, M. Lu, S. Yang, C. Xu, Z. Liu, J. Y. Lee, *ChemCatChem* **2016,** *8* (2), 372-379, (d) H. Kim, J. Park, I. Park, K. Jin, S. E. Jerng, S. H. Kim, K. T. Nam, K. Kang, *Nature Comm* **2015,** *6* (1), 8253.

9. (a) M. Pramanik, C. Li, M. Imura, V. Malgras, Y.-M. Kang, Y. Yamauchi, *Small* **2016,** *12* (13), 1709-1715, (b) Y. Zhou, H. C. Zeng, *Small* **2018,** *14* (21), 1704403.

10. Z. W. Seh, J. Kibsgaard, C. F. Dickens, I. Chorkendorff, J. K. Nørskov, T. F. Jaramillo, *Science* **2017,** *355* (6321), eaad4998.

11. D. Friebel, M. W. Louie, M. Bajdich, K. E. Sanwald, Y. Cai, A. M. Wise, M.-J. Cheng, D. Sokaras, T.-C. Weng, R. Alonso-Mori, R. C. Davis, J. R. Bargar, J. K. Nørskov, A. Nilsson, A. T. Bell, *J. Ame. Chem. Soc* **2015,** *137* (3), 1305-1313.

12. C. Tan, X. Cao, X.-J. Wu, Q. He, J. Yang, X. Zhang, J. Chen, W. Zhao, S. Han, G.-H. Nam, M. Sindoro, H. Zhang, *Chem. Rev* **2017,** *117* (9), 6225-6331.

13. L. Su, H. Du, C. Tang, K. Nan, J. Wu, C. Ming Li, *J. Colloid Interface Sci* **2018,** *528*, 36-44.

14. Y. Wan, H. Yang, D. Zhao, *Acc. Chem. Res* **2006,** *39* (7), 423-432.

15. (a) W. Liu, H. Liu, L. Dang, H. Zhang, X. Wu, B. Yang, Z. Li, X. Zhang, L. Lei, S. Jin, *Adv. Func. Mater* **2017,** *27* (14), 1603904, (b) M. W. Kanan, D. G. Nocera, *Science* **2008,** *321* (5892), 1072-1075, (c) R. D. L. Smith, M. S. Prévot, R. D. Fagan, S. Trudel, C. P. Berlinguette, *J. Ame. Chem. Soc* **2013,** *135* (31), 11580-11586.

16. D. Yang, Z. Lu, X. Rui, X. Huang, H. Li, J. Zhu, W. Zhang, Y. M. Lam, H. H. Hng, H. Zhang, Q. Yan, *Angew. Chem. Int. Ed* **2014,** *53* (35), 9352-9355.

17. F. B. Noronha, M. Schmal, B. Moraweck, P. Delichère, M. Brun, F. Villain, R. Fréty, *J. Phys. Chem. B* **2000,** *104* (23), 5478-5485.

18. (a) J. Yan, Z. Fan, W. Sun, G. Ning, T. Wei, Q. Zhang, R. Zhang, L. Zhi, F. Wei, *Adv. Func. Mater* **2012,** *22* (12), 2632-2641, (b) Y. Zhang, W. Sun, X. Rui, B. Li, H. T. Tan, G. Guo, S. Madhavi, Y. Zong, Q. Yan, *Small* **2015,** *11* (30), 3694-3702.

19. Y. Yin, P. Wu, H. Zhang, C. Cai, *Electrochem. Comm* **2012,** *18*, 1-3.

20. A. P. Grosvenor, M. C. Biesinger, R. S. C. Smart, N. S. McIntyre, *Surf. Sci* **2006,** *600* (9), 1771-1779.

21. C. Yan, Y. Zhu, Z. Fang, C. Lv, X. Zhou, G. Chen, G. Yu, *Adv. Ener. Mater* **2018,** *8* (23), 1800762.

22. C. S. Lim, C. K. Chua, Z. Sofer, K. Klímová, C. Boothroyd, M. Pumera, *J. Mater. Chem. A* **2015,** *3* (22), 11920-11929.

23. (a) D. Voiry, M. Chhowalla, Y. Gogotsi, N. A. Kotov, Y. Li, R. M. Penner, R. E. Schaak, P. S. Weiss, *ACS Nano* **2018,** *12* (10), 9635-9638, (b) C. C. L. McCrory, S. Jung, J. C. Peters, T. F. Jaramillo, *J. Ame. Chem. Soc* **2013,** *135* (45), 16977-16987.

24. D. Ge, J. Wu, G. Qu, Y. Deng, H. Geng, J. Zheng, Y. Pan, H. Gu, *Dalton. Trans* **2016,** *45* (34), 13509-13513.

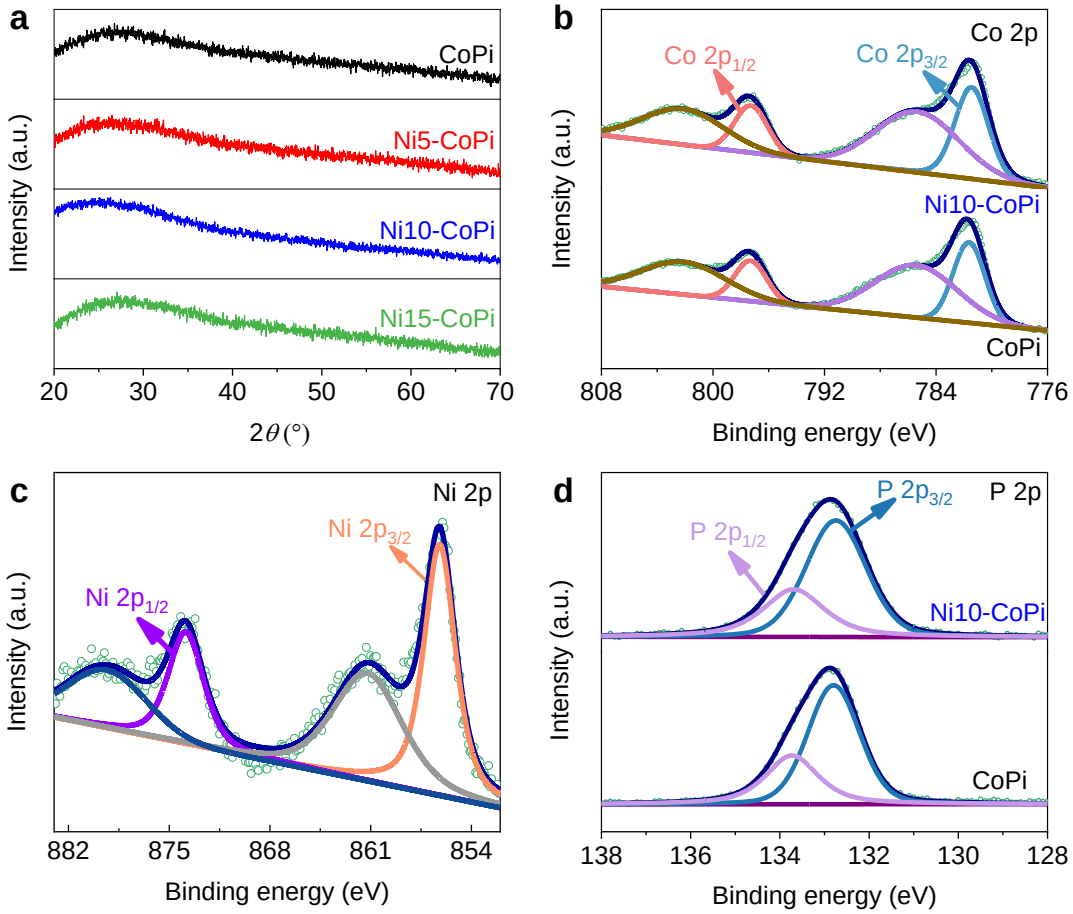


**Figure 1.** a) XRD patterns of CoPi (in orange), Ni5-CoPi (in blue), Ni10-CoPi (in black) and Ni15-CoPi (in red). XPS spectrums of CoPi and Ni10-CoPi in b) Co 2p region, c) Ni 2p region and d) P2p region.

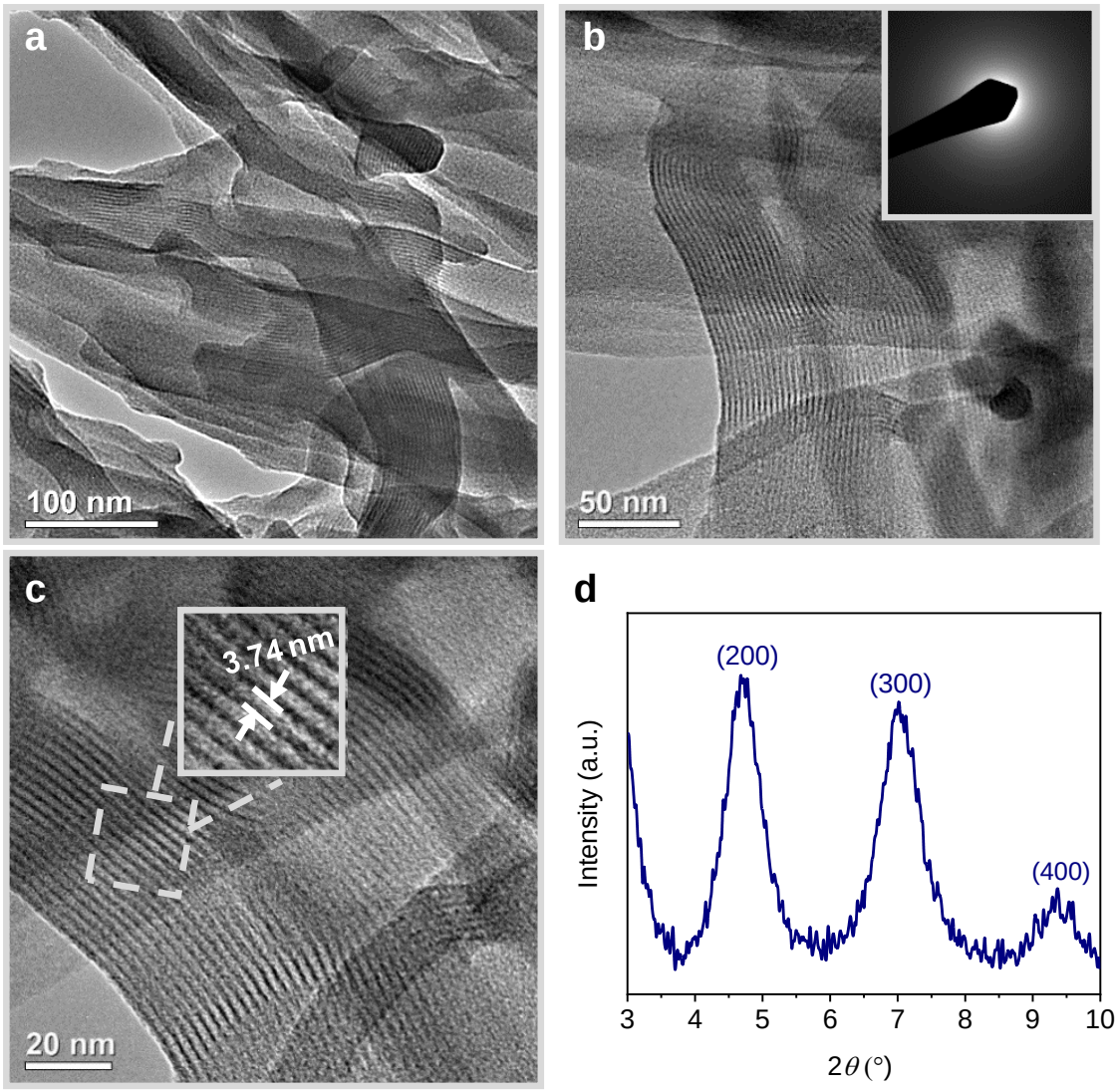


**Figure 2.** a) TEM image, b,c) HRTEM images, and d) Low-angle XRD pattern of Ni10-CoPi. The inset in (b) is the SAED pattern of Ni10-CoPi. The inset in (c) is the enlarged TEM image, showing the distance between neighboring channels is 3.74nm.

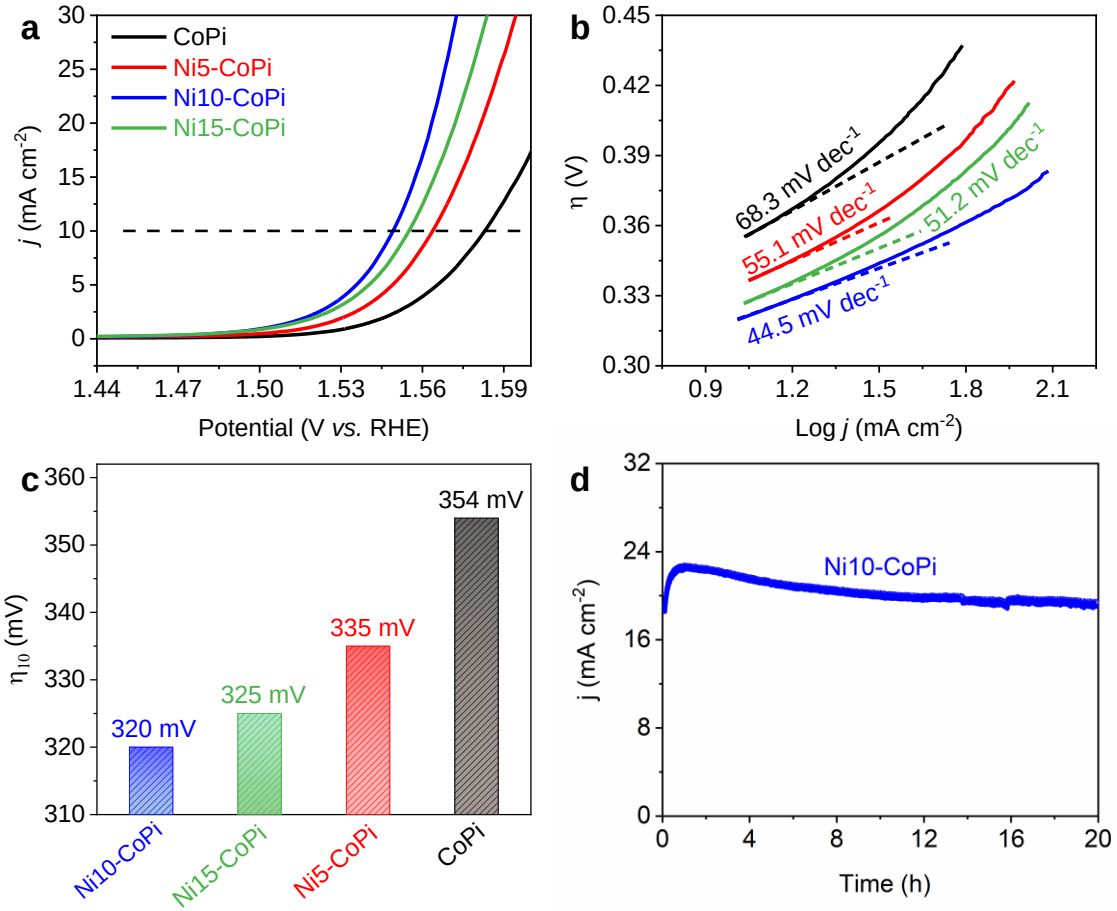


**Figure 3.** a) iR corrected OER polarization curves of CoPi, Ni5-CoPi, Ni10-CoPi, and Ni15-CoPi in 1.0 M KOH at scan rate of 2mV $s^{-1}$ and their corresponding b) Tafel Slope. c) The overpotentials of above samples at the current density of 10 mA $cm^{-2}$. d) The chronoamperometric measurements of Ni10-CoPi electrode under static overpotential (η=330 mV) for 20h.

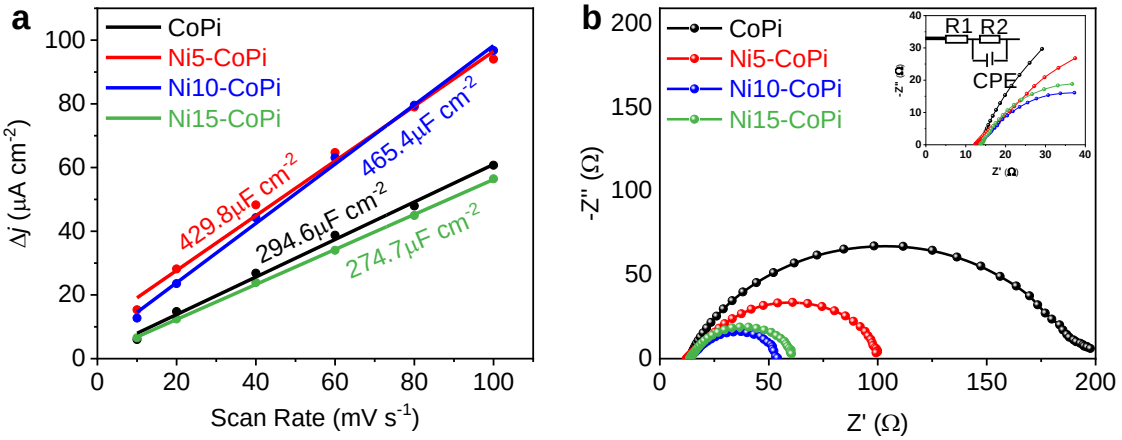


**Figure 4.** a) The charging current density differences ($\Delta j = j_{anodic} - j_{cathodic}$) plotted against scan rates of the as-prepared CoPi, Ni5-CoPi, Ni10-CoPi and Ni15-CoPi electrodes. b) EIS spectrum measured at 340 mV overpotential of CoPi, Ni5-CoPi, Ni10-CoPi and Ni15-CoPi.